Supporting Information for

Sulfonate-Assisted Surface Iodide Management for High-Performance Perovskite Solar Cells and Modules

Ruihao Chen, Yongke Wang, Siqing Nie, Hui Shen, Yong Hui, Jian Peng, Binghui Wu, Jun Yin,* Jing Li* and Nanfeng Zheng

Pen-Tung Sah Institute of Micro-Nano Science and Technology, OSED, Jiujiang Research Institute, State Key Laboratory for Physical Chemistry of Solid Surfaces, Collaborative Innovation Center of Chemistry for Energy Materials, National & Local Joint Engineering Research Center of Preparation Technology of Nanomaterials, Innovation Laboratory for Sciences and Technologies of Energy Materials of Fujian Province, College of Chemistry and Chemical Engineering, Xiamen University, Xiamen 361005, China.

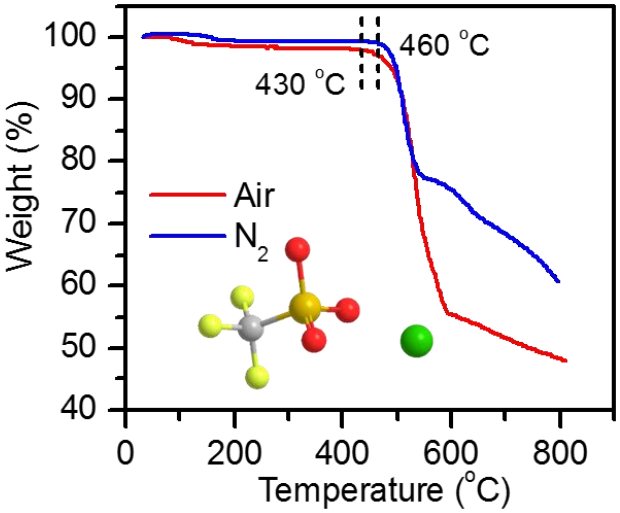

Figure S1. Thermogravimetric (TG) analysis of $CsCF_3SO_3$ powder. It can be seen that the decomposition temperature of $CsCF_3SO_3$ no matter in nitrogen or air both exceeds 400°C, indicating its excellent thermal stability. Inset is the ball-stick model of $CsCF_3SO_3$ (green ball is Cs, orange ball is S, grey ball is C, yellow ball is F and red ball is O).

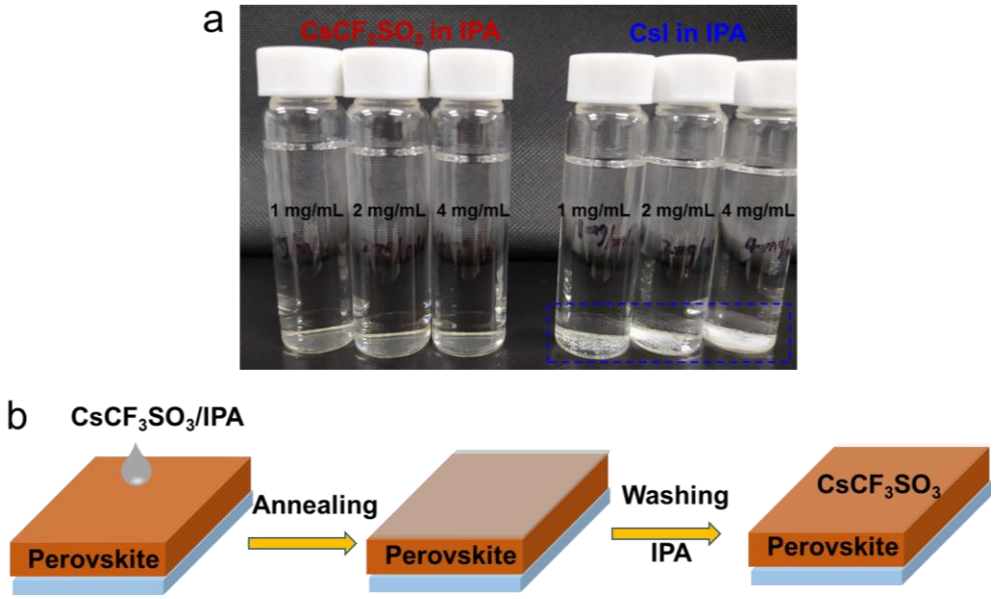

Figure S2. (a) Solubility of $CsCF_3SO_3$ with comparison of CsI powders in IPA. (b) Schematic illustration of the $CsCF_3SO_3$ post-treatment process. The results show that CsI is almost insoluble in IPA, while $CsCF_3SO_3$ has good solubility in isopropanol, and the solubility range is 0-4 mg/mL. Thus, $CsCF_3SO_3$ solutions can be blade-coated or spin-coated onto the surface of perovskite films.

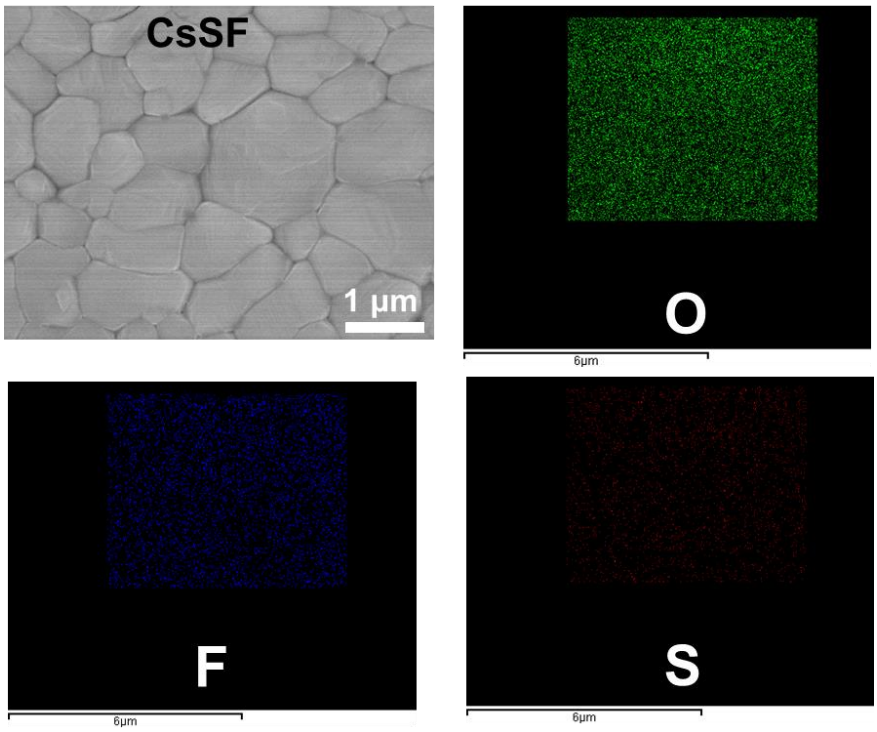

Figure S3. Top-view SEM image and EDS mappings of the CsSF film for O, F and S elements.

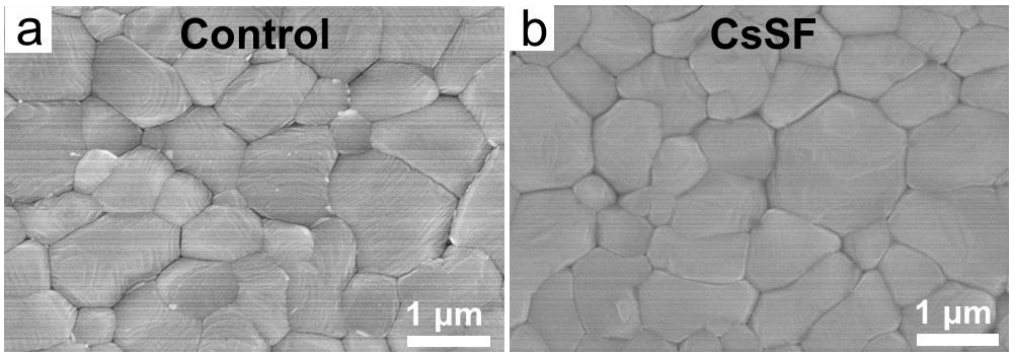

Figure S4. Top-view SEM images of the prepared (a) Control and (b) CsSF films.

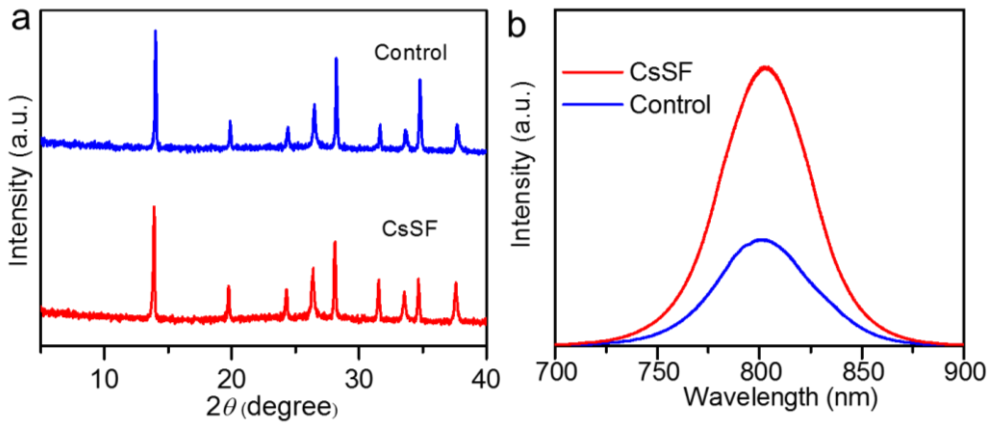

Figure S5. (a) XRD patterns and (b) PL spectra of the Control and CsSF perovskite films.

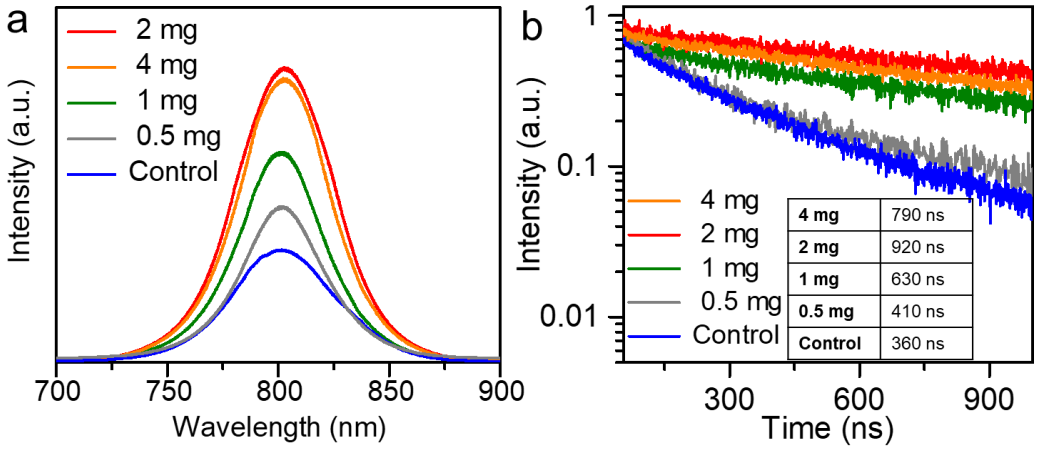

Figure S6. (a) PL and (b) TRPL spectra of the perovskite films without and with $CsCF_3SO_3$ treatment in different concentration in isopropanol (0.5, 1, 2 and 4 mg/mL). The best $CsCF_3SO_3$ concentration was demonstrated to be 2 mg/mL. The corresponding average decay time was summarized in the inset table.

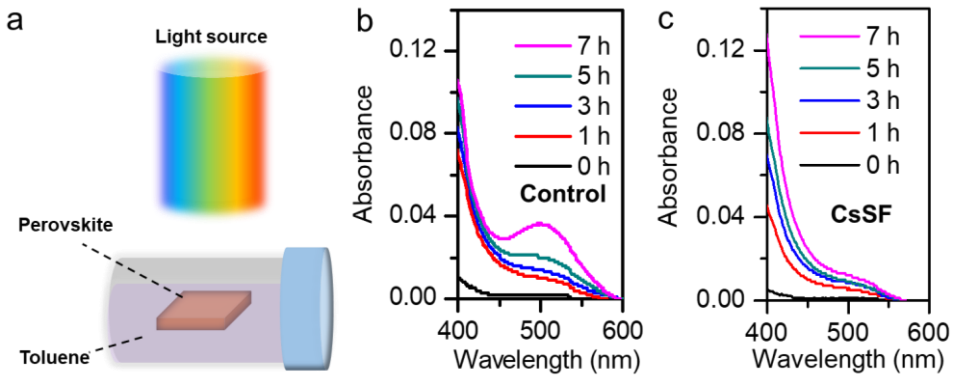

Figure S7. Iodine-loss analysis of the perovskite films. (a) Schematic illustration of the iodine-loss experimental setup: vials filled and sealed in nitrogen, containing perovskite films fully submerged in toluene, were exposed to AM 1.5G irradiation at ~55°C. Ten UV-vis absorbance spectra recorded for the toluene solution taken from the (b) Control and (c) CsSF films vials with different aging durations.

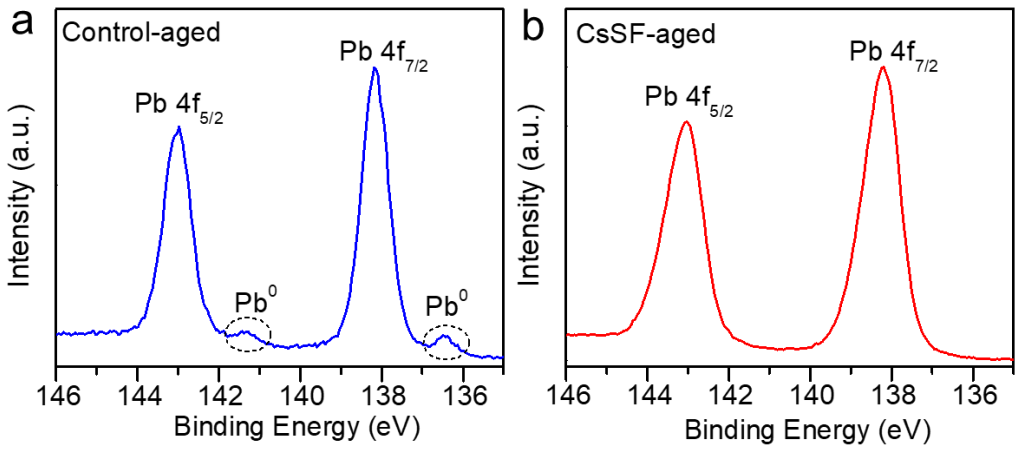

Figure S8. High-resolution XPS spectra of Pb 4f for the aged Control (a) and (b) CsSF perovskite films being exposed to AM 1.5G illumination in N_2 for 24 hours.

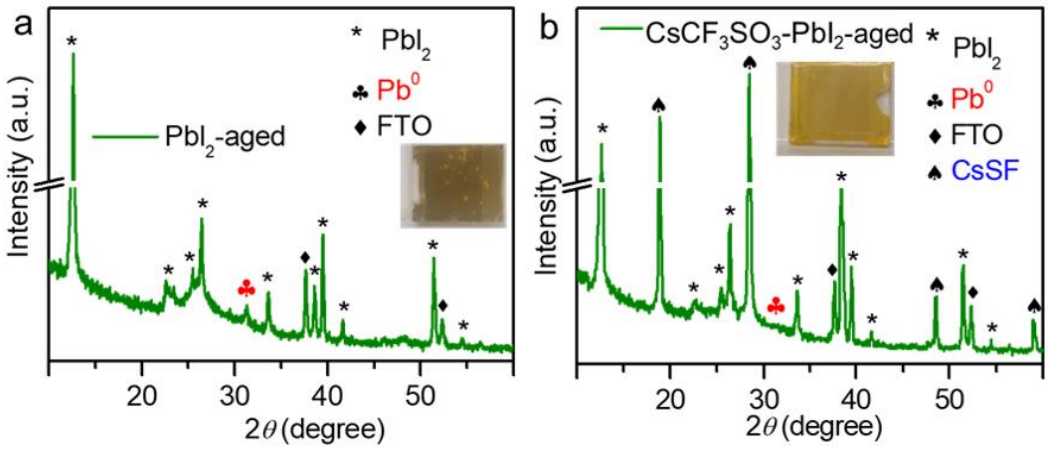

Figure S9. Evolution of XRD patterns of (a) PbI_2 and (b) $CsCF_3SO_3$-PbI_2 films measured after aging under AM 1.5G irradiation at 85˚C in a nitrogen filled glove box. Insets are the digital images of the aged PbI_2 and $CsCF_3SO_3$-PbI_2 films. The results showed that after 50 h, metallic Pb^0 was detected in the PbI_2 film, which can be attributed to the conversion of PbI_2 to metal Pb and release I_2. While the metal Pb was not detected in the $CsCF_3SO_3$-PbI_2 film, which evidences that $CsCF_3SO_3$ can effectively stabilize the PbI_2 frame structure. This also proved that $CsCF_3SO_3$ could improve the light and thermal stabilities of perovskite by inhibiting the formation of I_2.

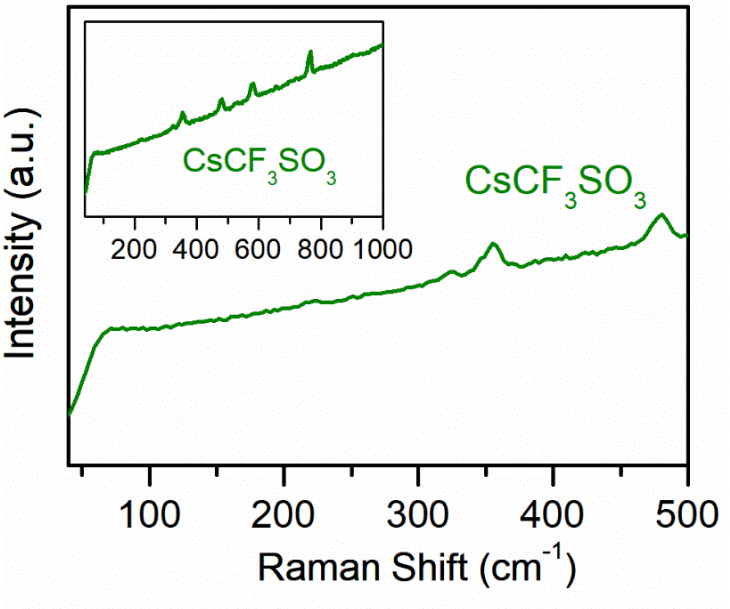

Figure S10. Raman spectrum of the pure $CsCF_3SO_3$ powder.

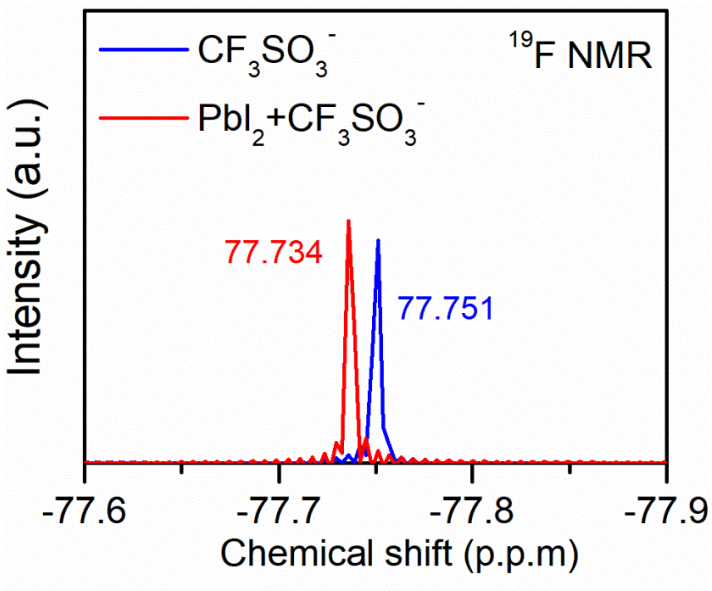

Figure S11. ^{19}F NMR spectra of pure $CsCF_3SO_3$ powder and $CsCF_3SO_3$ with PbI_2 dissolved in DMSO-d_6.

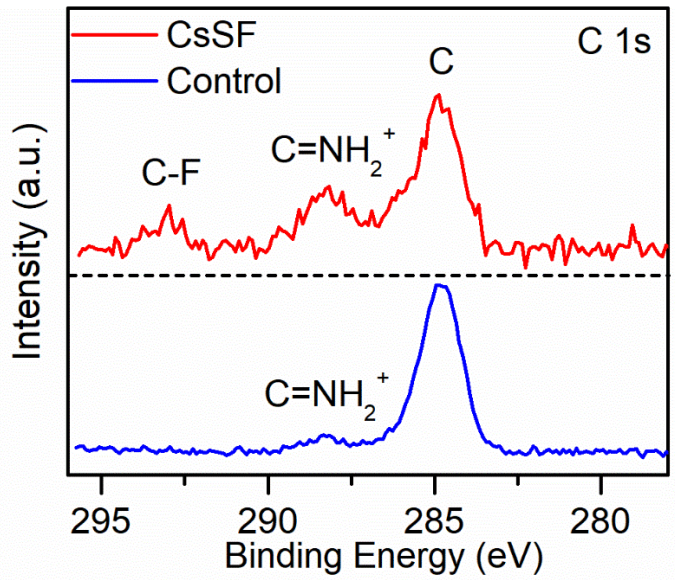

Figure S12. High-resolution XPS C 1s spectra of the Control and CsSF films. The existence of strong peak (284.8 eV) in the C 1s spectra from the two samples is attributed to the surface contaminations during the ex-situ preparation of the samples. The contaminative carbon (284.8 eV) was also used as a certain reference element to calibrate the peak positions of else elements.[1] The CsSF film gives a broad specific

peak at a binding energy of 293.2 eV in the C 1s spectra indicating the -CF_3 group in the $CF_3SO_3^-$ ions.

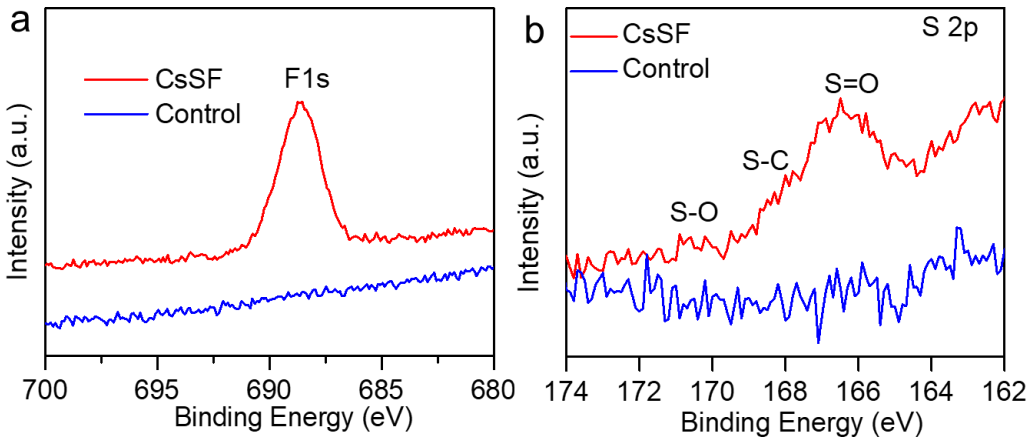

Figure S13. High-resolution XPS spectra of (a) F 1s and (b) S 2p peaks of the Control and CsSF films.

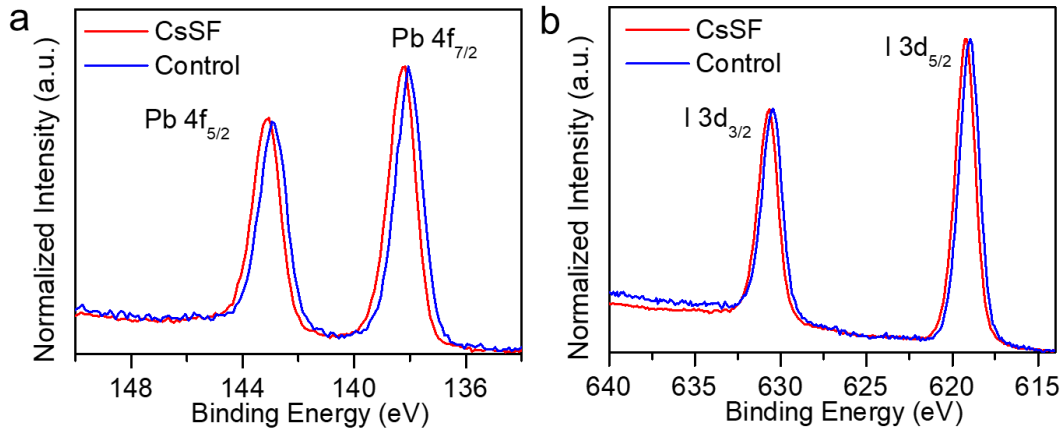

Figure S14. XPS spectra of (a) Pb 4f and (b) I 3d peak of the Control and CsSF films. Compared with the Control film, the peak positions of Pb $4f_{7/2}$ and Pb $4f_{5/2}$ for CsSF films both shifted to higher binding energy, and the peaks of I $3d_{3/2}$ and I $3d_{5/2}$ also shifted slightly with the same trend due to the stronger electronegativity of oxygen.

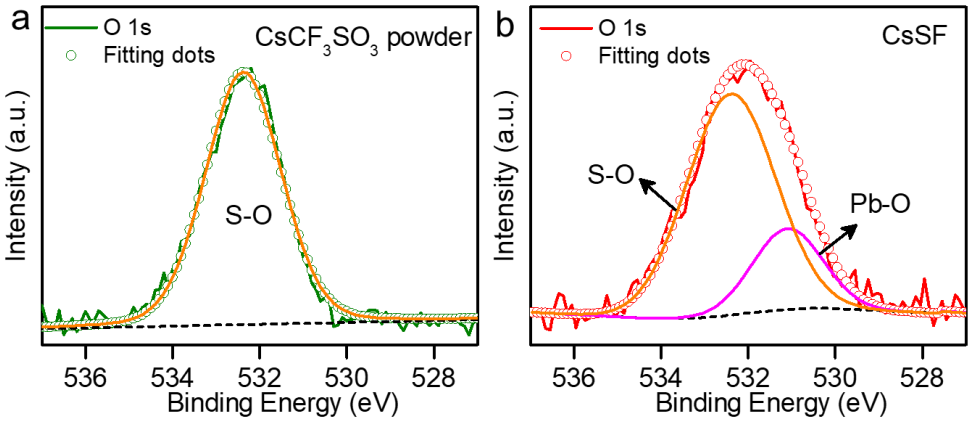

Figure S15. High-resolution XPS O 1s curves of (a) $CsCF_3SO_3$ powder and (b) CsSF film. There is one chemical state for surface oxygen atoms (S-O) in the $CsCF_3SO_3$ powder, while a new additional chemical state (Pb-O) appeared in the CsSF film which indicated the strong interaction between $CF_3SO_3^-$ and Pb^{2+} ions.

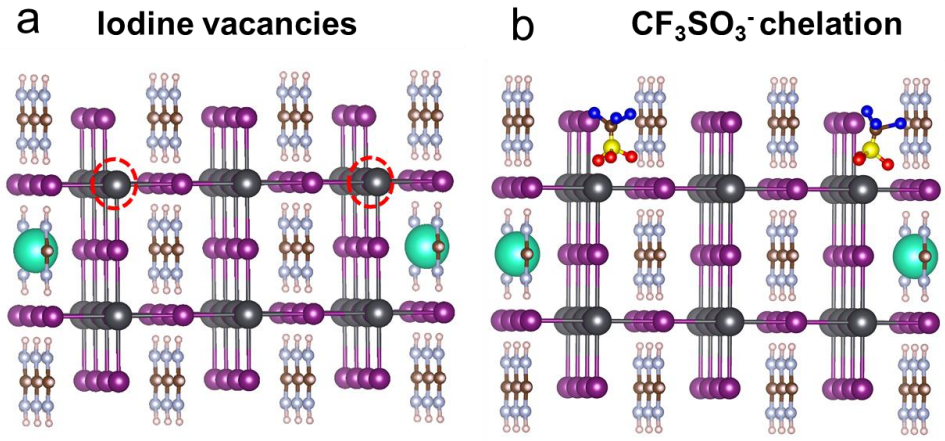

Figure S16. Scheme of the surface model of (a) Control and (b) CsSF perovskite films (purple ball is I, green ball is Cs, blue ball is F, black ball is Pb, brown ball is C, grey ball is N, yellow ball is S, red ball is O, and pink ball is H). The binding energies of CsSF and Control perovskite were further estimated by employing density functional theory (DFT) based first-principal calculations. The calculated binding energy (-1.382 eV) of the perovskite films treated by $CF_3SO_3^-$ was stronger than that of the untreated surface (-1.061 eV), which indicates that $CF_3SO_3^-$ is conducive to the formation of a more stable surface.

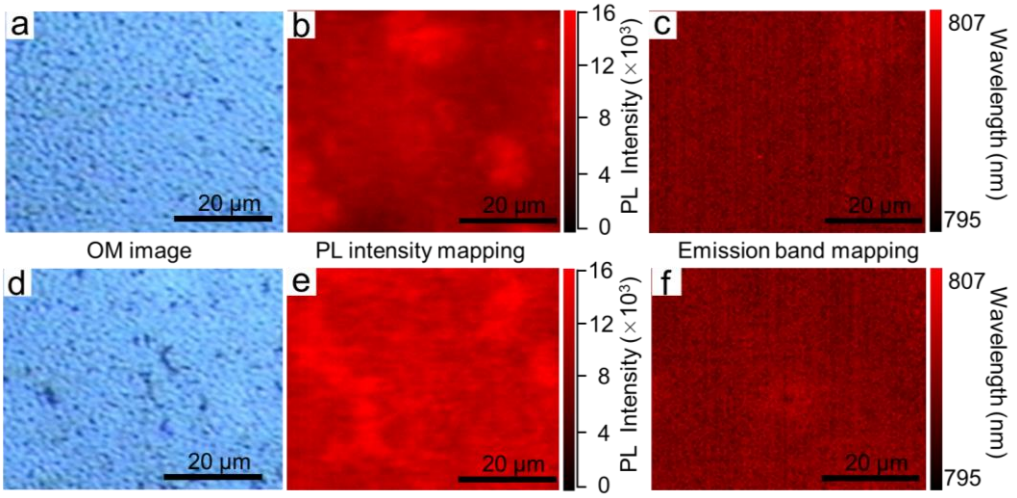

Figure S17. Optical morphology **(**OM) images, the corresponding PL mapping (excited at 532 nm) and emission wavelength mapping (excited at 532 nm) of the Control film (a-c) and CsSF film (d-f) in a large-area region.

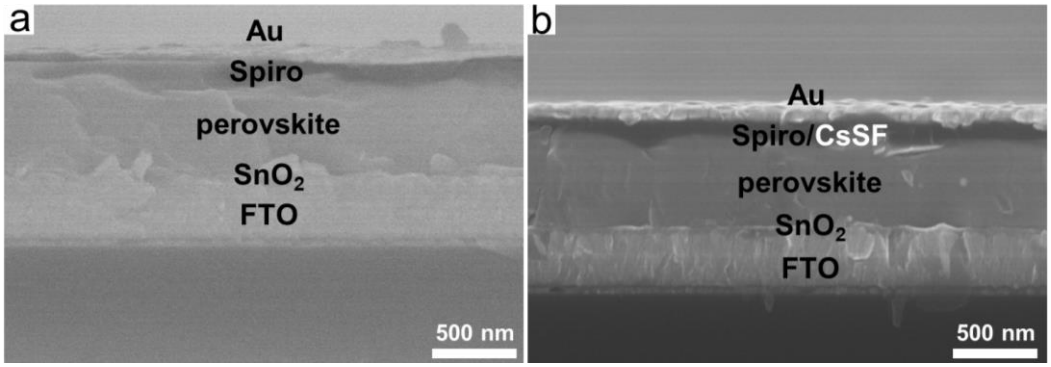

Figure S18. Cross-sectional SEM images of the (a) Control and (b) CsSF film-based PSCs, respectively.

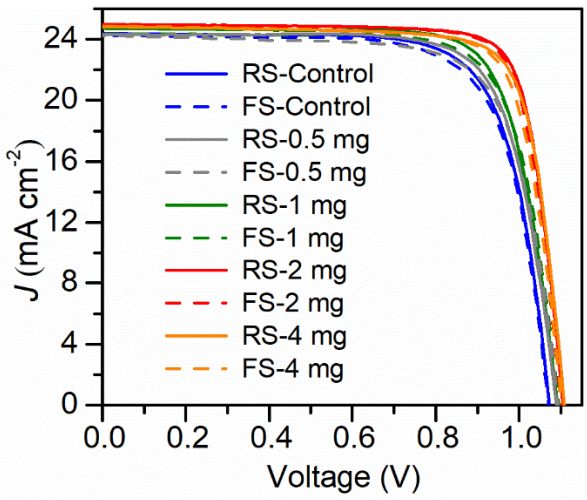

Figure S19. *J-V* curves for the PSCs without and with $CsCF_3SO_3$ in different concentrations.

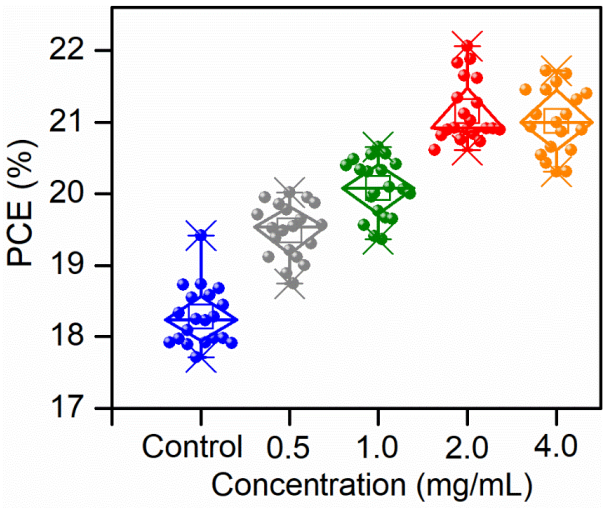

Figure S20. PCE statistics of 20 individual PSCs without and with $CsCF_3SO_3$ in different concentrations. In a limited range of solubility (≤ 4 mg/mL), it is understandable that the low concentration (0.5, 1 mg/mL) of $CsCF_3SO_3$ would lead to the insufficient modification of perovskites, resulting the less improvement in PV performance. Furthermore, the efficiencies of the devices are relatively close when the perovskite film is treated at a concentration of 2, 4 mg/mL, which indicates that the surface substitution of iodide ion has reached equilibrium. The possible reason should be that the additional residual salt can be removed easily in the subsequent IPA washing process without disturbing the interfacial charge transport.

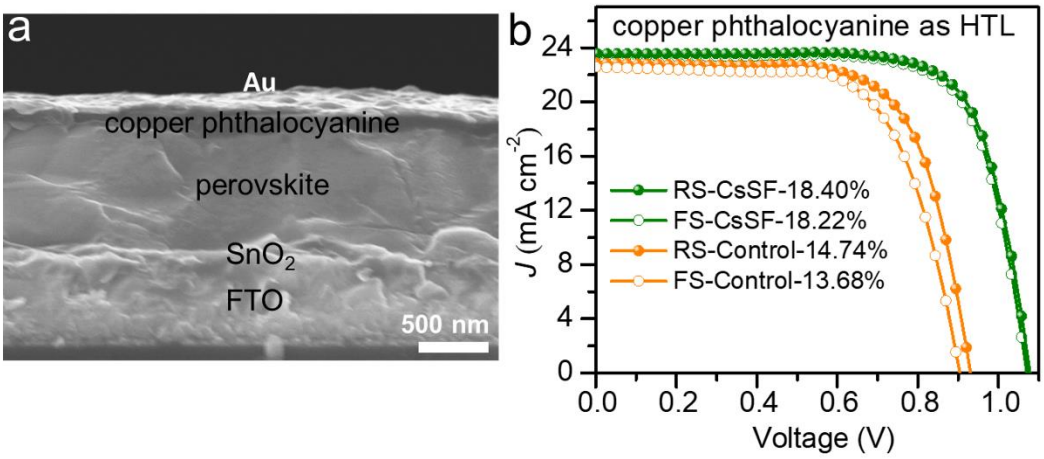

Figure S21. (a) Cross-sectional SEM image of the typical device structure using the copper phthalocyanine as HTL. (b) *J-V* curves of the Control and CsSF devices based on copper phthalocyanine as HTL.

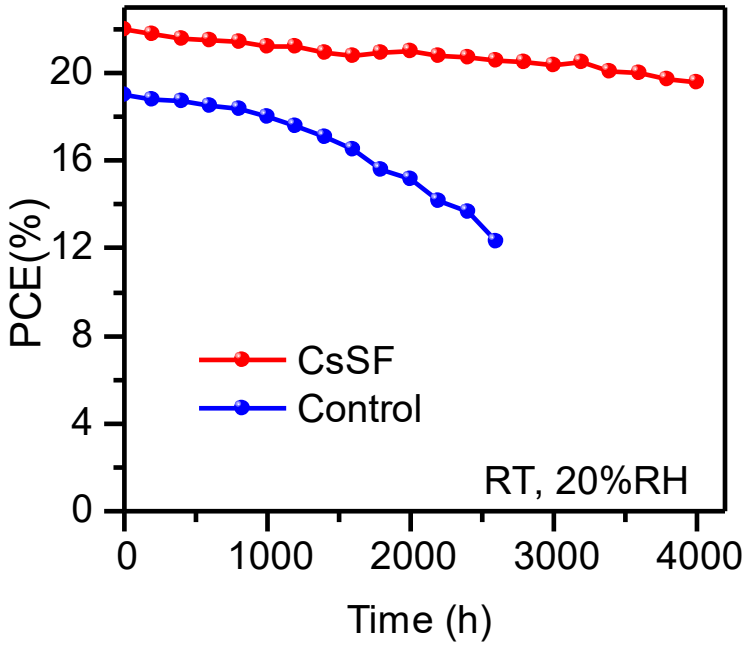

Figure S22. Moisture stability of CsSF and Control PSCs under storage condition (25°C, 20% RH). It can be seen that the CsSF PSC retained 90% of the initial PCE value after 4000 h.

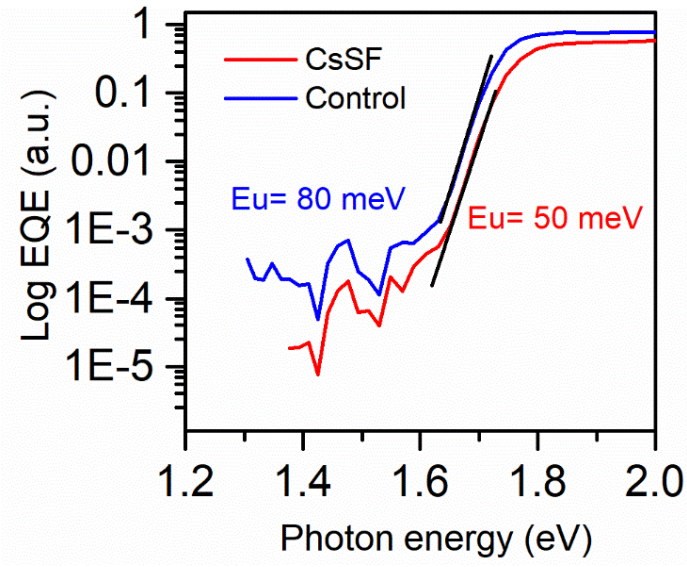

Figure S23. Semi-log plot of the IPCE spectra versus photon energy for the best-performing solar cells based on CsSF and Control films. The slope of the exponential IPCE tail defines the Urbach energy (E_u) according to the equation of IPCE = $IPCE_0$ exp [(E-E_g)/$_{Eu}$], where $IPCE_0$ is the IPCE value at the bandgap (E_g).

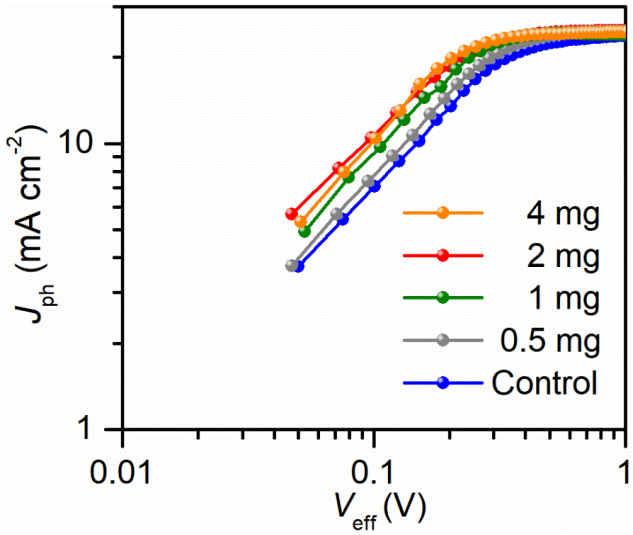

Figure S24. J_{ph}-V_{eff} curves for the PSCs without and with $CsCF_3SO_3$ treatment in different concentrations. The photocurrent density (J_{ph}, defined as J_{sc}-J_D, where J_{sc} and J_D were the photogenerated densities under AM 1.5G 100 mW cm^{-2} illumination and in the dark, respectively.) versus the effective voltage (V_{eff}, defined as V_0-V, where V was the applied voltage, and V_0 was the voltage when J_{ph} = 0) was plotted. All the devices with different $CsCF_3SO_3$ amount have higher J_{ph} superior to the Control device, which also reflects a more efficient charge extraction in the perovskite/HTL interface.

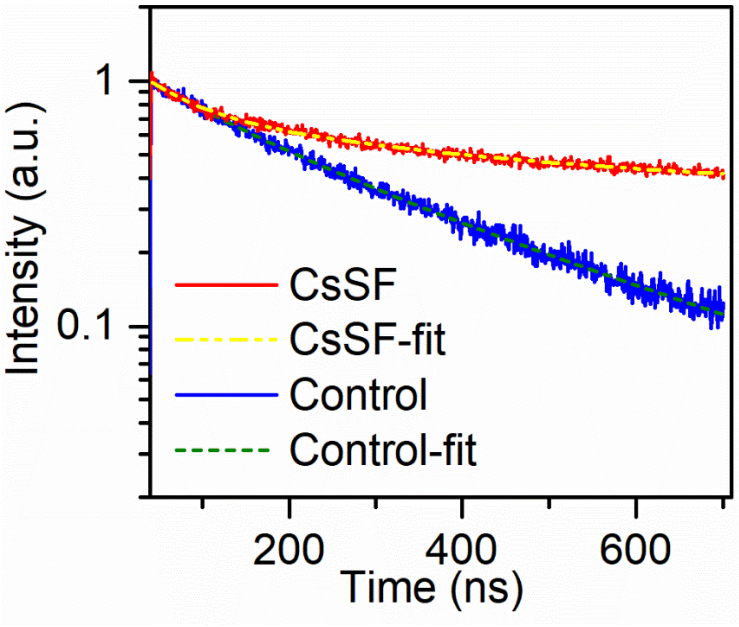

Figure S25. TRPL spectra of Control and CsSF films deposited on glass substrate.

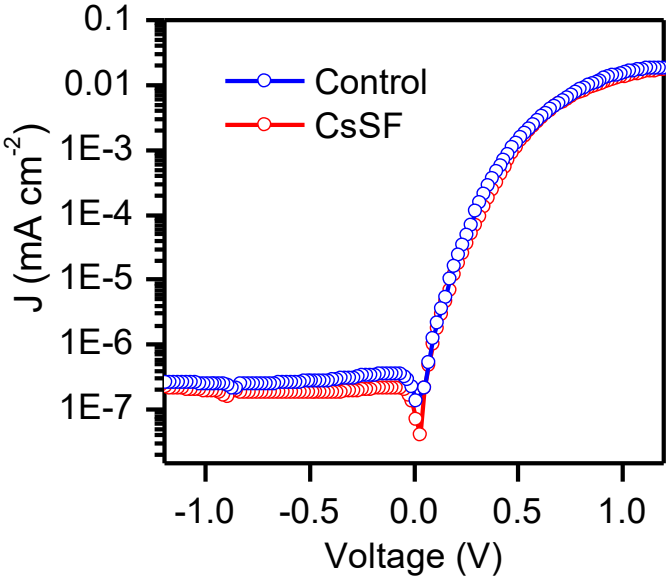

Figure S26. *J–V* curves of PSCs prepared by the CsSF film compared with those by the Control film at the reverse scan with the scan rate of 50 mV s^{-1} under dark conditions.

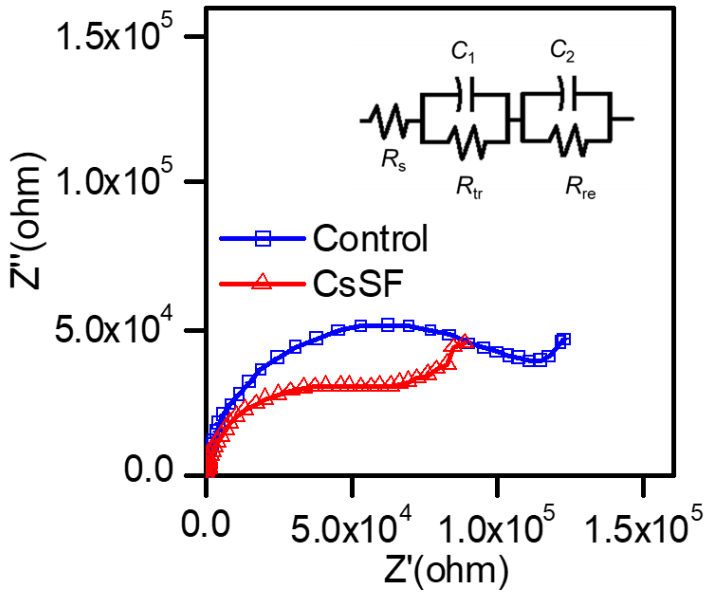

Figure S27. Electrochemical impedance spectroscopy (EIS) characteristics of the champion cells with Control or CsSF films. The Nyquist plots for the PSCs based on Control or CsSF films were measured at 0 V bias under dark conditions. Inset shows the corresponding equivalent circuit. By fitting the semicircle at high frequency region, it was found that the $CF_3SO_3^-$ treatment substantially reduced the charge transfer resistance R_{ct} from 1.5×10^4 to 4.6×10^3 Ω. The smaller R_{ct} suggests that the corresponding charge transfer for the device is much more efficient than the reference one. Moreover, the recombination resistance R_{rec} derived from the low frequency region was increased from 2.2×10^4 to 2.6×10^5 Ω after $CsCF_3SO_3$ chelation.

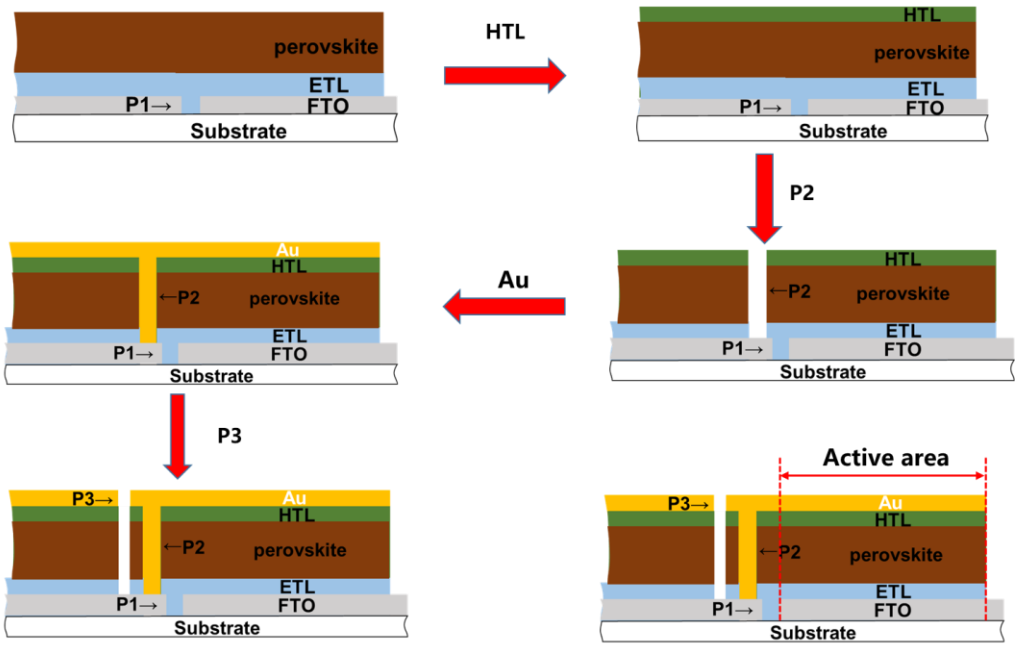

Figure S28. Schematic illustration of the laser-scribing (P1, P2, P3) process for PSC modules.

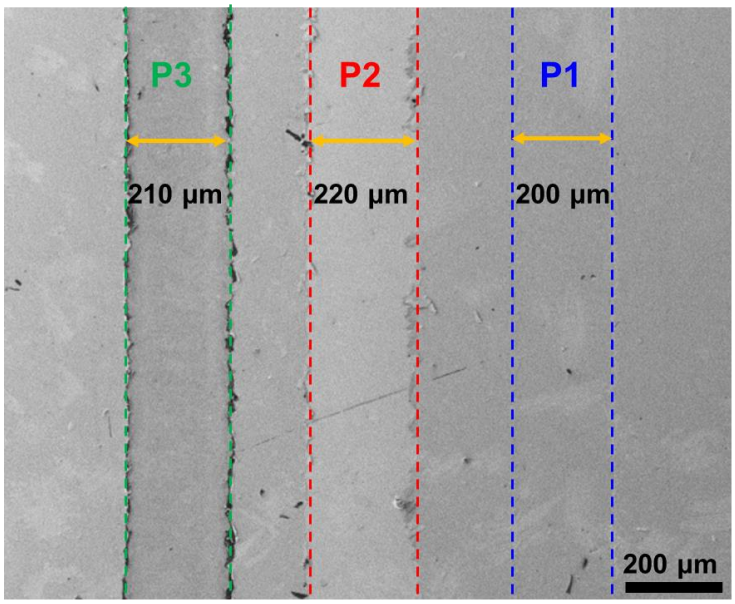

Figure S29. SEM image of the 100-cm^2 solar module showing the P3-P2-P1 parameters.

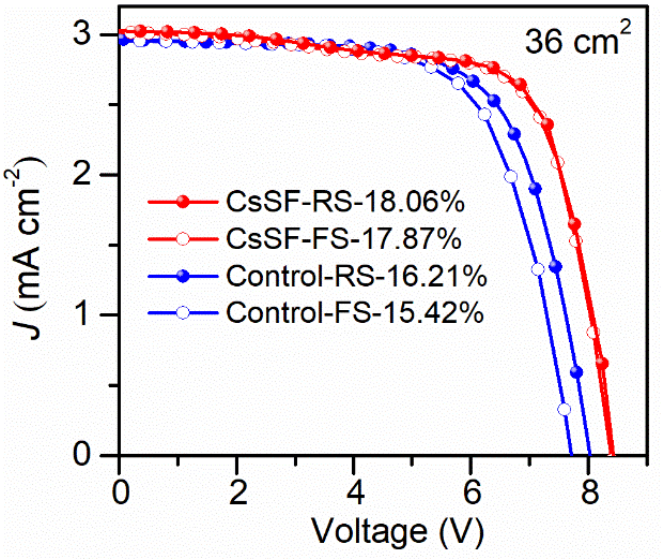

Figure S30. *J-V* characteristics of the Control and CsSF PSC modules with 36-cm^2 area.

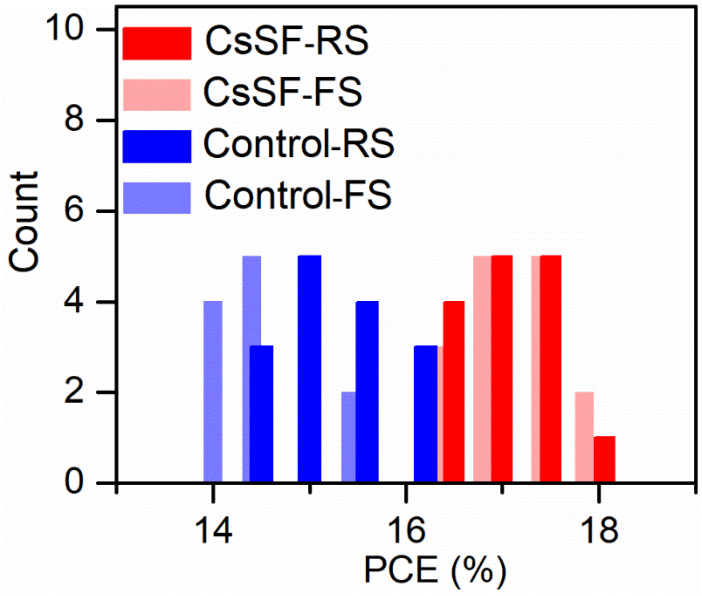

Figure S31. PCE distribution of 15 solar modules (36 cm^2) based on the Control and CsSF films.

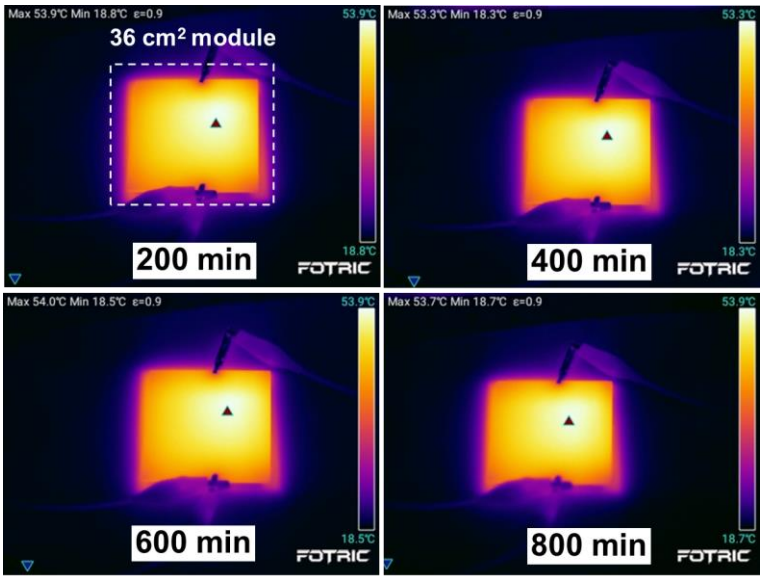

Figure S32. Thermal images of the 36-cm^2 PSC module captured by a thermal imaging camera (Fotric 236) with the different time under maximum power point tracking and AM 1.5G illumination at RH 60%. The temperature of the modules was measured to be ~54 °C due to the heating effect of the solar irradiation.

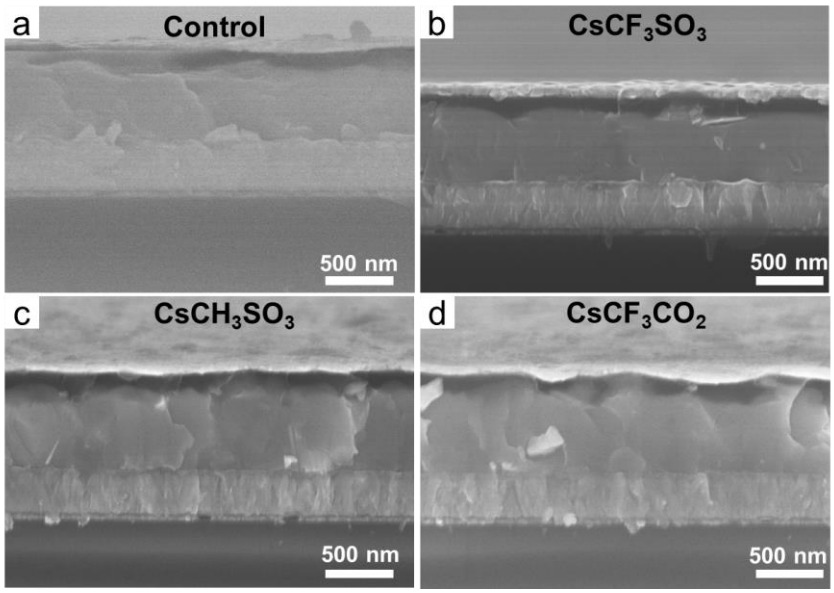

Figure S33. Cross-sectional SEM images of the (a) Control, (b) $CsCF_3SO_3$, (c) $CsCH_3SO_3$ and (d) $CsCF_3CO_2$ film-based PSCs, respectively.

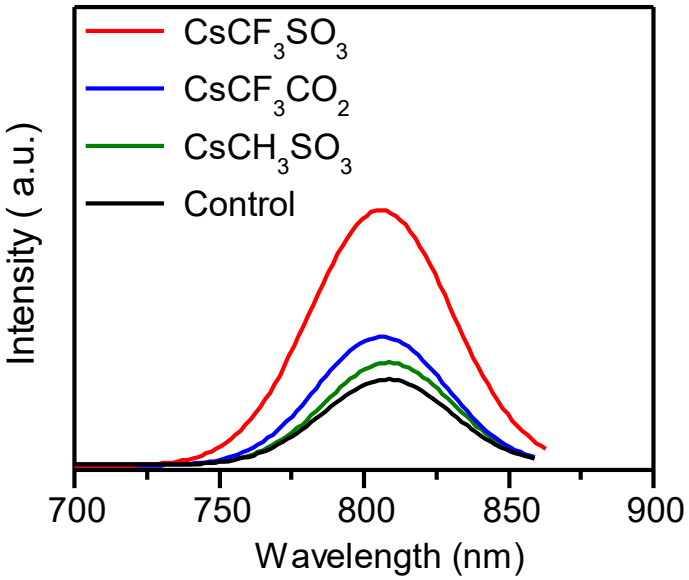

Figure S34. Steady PL spectra of the Control, $CsCF_3SO_3$, $CsCH_3SO_3$ and $CsCF_3CO_2$ films, respectively.

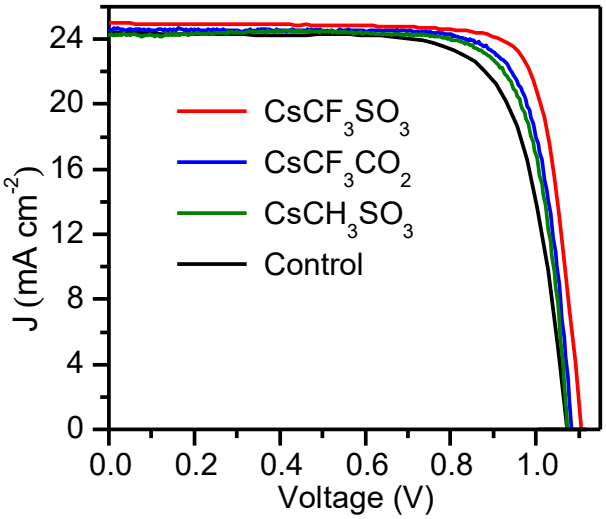

Figure S35. *J-V* characteristics of the champion cells using $CsCF_3SO_3$, methanesulfonate ($CsCH_3SO_3$), trifluoroacetate ($CsCF_3CO_2$) to treat the perovskite films. In this work, the selected structure of $CF_3SO_3^-$ with F group was used to improve the stability of perovskite film and corresponding devices. Also, the more oxygen atoms of $CF_3SO_3^-$ than previously reported $CF_3CO_2^-$ can offer more active site to more effectively interact with Pb^{2+} ions. Thus, $CF_3SO_3^-$ structure was the optimized among the kinds of oxygen-containing structure.

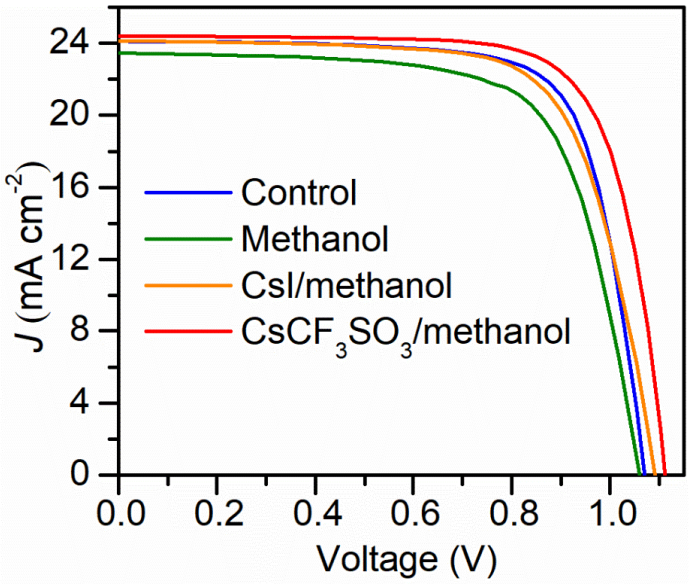

Figure S36. *J-V* characteristics of the champion cells using $CsCF_3SO_3$/methanol, CsI/methanol, and methanol to treated the perovskite films. Due to possible damaging of methanol for perovskites, the Control device treated by methanol demonstrates an obviously reduced the efficiency (17.33%) which is lower than that of the pristine one (19%). While in the same concentration (20 mM for Cs^+) for $CsCF_3SO_3$, the efficiency of the device can achieve to 20.04%, which is higher than that of the device with CsI (18.59%) and the pristine device (19%). Obviously, different from the ion compensation effect from CsI with improved photovoltaic performance, the surface defects' (iodide vacancies) repair or passivation by $CF_3SO_3^-$ exhibits much important roles for the efficient carriers' transport for the better efficiency.

Table S1. Photovoltaic parameters of PSCs (0.12 cm^2 of active area).

Device		J_{sc}/mA·cm^{-2}	V_{oc}/V	*FF*/%	η/%
CsSF	Reverse	24.97	1.11	80.01	22.06
	Forward	24.97	1.11	79.85	21.89
Control	Reverse	24.40	1.07	74.31	19.42
	Forward	24.27	1.07	73.11	18.97

Table S2. Photovoltaic parameters of PSCs (0.12 cm^2 of active area) with different concentrations of $CsCF_3SO_3$.

Device		J_{sc}/mA·cm^{-2}	V_{oc}/V	*FF*/%	η/%
Control	Reverse	24.40	1.07	74.31	19.42
	Forward	24.27	1.07	73.11	18.97
0.5 mg	Reverse	24.30	1.09	75.59	20.02
	Forward	24.24	1.09	73.25	19.35
1 mg	Reverse	24.71	1.09	76.67	20.65
	Forward	24.37	1.09	75.95	20.17
2 mg	Reverse	24.97	1.11	80.01	22.06
	Forward	24.97	1.11	79.85	21.89
4 mg	Reverse	24.87	1.11	78.68	21.72
	Forward	24.82	1.10	77.91	21.27

Table S3. Photovoltaic parameters of PSCs based on Cupc HTL (0.12 cm^2 of active area).

Device		J_{sc}/mA·cm^{-2}	V_{oc}/V	*FF*/%	η/%
CsSF	Reverse	23.55	1.07	73.00	18.40
	Forward	23.41	1.07	72.72	18.22
Control	Reverse	22.83	0.93	69.41	14.74
	Forward	22.67	0.90	67.04	13.68

Table S4. Photovoltaic parameters of solar modules (18 cm^2 of active area).

Device		J_{sc}/mA·cm^{-2}	V_{oc}/V	*FF*/%	η/%
CsSF	Reverse	3.02	8.43	70.94	18.06
	Forward	3.02	8.39	70.55	17.87
Control	Reverse	2.97	8.02	68.08	16.21
	Forward	2.96	7.72	67.49	15.42

Table S5. Photovoltaic parameters of the CsSF PSC module (47 cm^2 of active area).

Device	J_{sc}/mA·cm^{-2}	V_{oc}/V	*FF*/%	η/%
Reverse	1.68	13.3	70.31	15.71
Forward	1.70	12.8	62.59	13.62

Table S6. Photovoltaic parameters of PSCs (0.12 cm^2 of active area).

Device	J_{sc}/mA·cm^{-2}	V_{oc}/V	*FF*/%	η/%
Control	24.40	1.07	74.31	19.42
$CsCF_3SO_3$	24.97	1.11	80.01	22.06
$CsCH_3SO_3$	24.29	1.07	77.76	20.21
$CsCF_3CO_2$	24.61	1.08	78.38	20.83

Table S7. Photovoltaic parameters of PSCs (0.12 cm^2 of active area).

Device	J_{sc}/mA·cm^{-2}	V_{oc}/V	*FF*/%	η/%
Control	24.10	1.07	73.66	19.00
Methanol	23.50	1.06	69.58	17.33
CsI/methanol	24.15	1.09	70.90	18.66
$CsCF_3SO_3$/methanol	24.41	1.11	74.45	20.17

Notes:

In the HS-LEISS measurement, due to the fixed test area, the average areal density of surface atoms is approximately unchanged. Since Ne^+ ions have different sputtering efficiencies for the relatively small atomic number elements (C, H and N) and large atomic number elements (Pb and I), C, H and N elements are more likely to be sputtered and etched detaching, which increases the relative percentage of Pb and I elements on the perovskite surface, and thus enhances the peak intensity of Pb and I elements. Nevertheless, the atom ratio of the Pb/I tends to be stable during the sputtering process.

References

1. Chen, S. S.; Deng, Y. H.; Gu, H. Y.; Xu, S.; Wang, S.; Yu, Z. H.; Blum, V.; Huang, J. S. Trapping lead in perovskite solar modules with abundant and low-cost cation-exchange resins. *Nat. Energy* 2020, **5**, 1003-1011.